PHYSICOCHEMICAL ANALYSIS
OF INORGANIC SYSTEMS

Phase Relations in the ZrO_2–FeO System

S. V. Beshta*, E. V. Krushinov*, V. I. Al'myashev**, S. A. Vitol'*,
L. P. Mezentseva**, Yu. B. Petrov***, D. B. Lopukh***, V. B. Khabenskii*,
M. Barrachin****, S. Hellmann*****, and V. V. Gusarov**

Aleksandrov Research Technological Institute, Sosnovyi bor, Leningrad oblast, Russia

** Grebenshchikov Institute of Silicate Chemistry, Russian Academy of Sciences,
ul. Odoevskogo 24/2, St. Petersburg, 199155 Russia*

*** St. Petersburg Electrotechnical University (LETI), St. Petersburg, Russia*

**** Institut de Radioprotection et de Sûreté Nucleair (IRSN), Paris, France*

***** FRAMATOME ANP, Erlangen, Germany*

Received March 15, 2005

Abstract—We present the results of the investigation of the ZrO_2–FeO system under an inert atmosphere. We have refined the position of the eutectic point, which lies at $1332 \pm 5°C$ and 10.3 ± 0.6 mol % ZrO_2. The iron oxide solubility boundaries in zirconium dioxide have been determined over a wide temperature range taking into account the polymorphism in ZrO_2. A phase diagram for the system has been designed.

Iron and zirconium oxides are important components of many inorganic materials. The systems containing zirconium dioxide are interesting because of the high fire resistance, strength, crack resistance, chemical inertness, oxygen superionic conductivity, and other essential properties of zirconia-containing materials [1]. In addition, the systems in which ZrO_2 and FeO are major components are significant for understanding whether refractories would react with metallurgical slag [2] and whether the melt in the active zone of a nuclear reactor would react with its housing material [3, 4] and with the device designed to keep the melt in the active zone of a reactor in cases of severe nuclear accidents [5, 6]. In this respect, any data on the ZrO_2–FeO system are of great importance for the prediction of phase and chemical transformations over a wide temperature range in the aforementioned multicomponent systems.

One who researches phase equilibria in a ZrO_2–FeO system has to overcome several methodological difficulties; this system remains poorly studied for this reason. Above all, the design of the ZrO_2–FeO phase diagram is complicated by polymorphism and the high melting point of ZrO_2. Three structural polymorphs of zirconia exist at different temperatures under normal pressure: monoclinic m-ZrO_2, tetragonal t-ZrO_2, and cubic c-ZrO_2 [1, 7]. The m-$ZrO_2 \longrightarrow t$-ZrO_2 and t-$ZrO_2 \longrightarrow c$-ZrO_2 polymorphic transition temperatures are 1172 and 2347°C, respectively; the melting temperature is 2710°C [8]. The dependence of the phase state and composition of iron-containing phases on the oxygen partial pressure [8–14] (Fig. 1) is another

significant factor complicating the investigation of phase equilibria in the system in question.

We examined the data compiled in [15] and found that only one work has concerned the phase diagram of the ZrO_2–FeO system. Fischer and Hoffman [16] investigated the system at moderate temperatures (up to 1800°C). They discovered the following features in the system: a eutectic point at 1.8 mol % ZrO_2 and $1330 \pm 15°C$, a ZrO_2-based solid solution (ss) field with an extent of 6.7 mol % FeO at 1450°C and 5 mol % FeO at 1800°C; these ss were structurally studied using single-crystal X-ray diffraction, and their unit cell parameters were determined [16].

EXPERIMENTAL

The starting chemicals used for sample preparation are pure grade ZrO_2 (>99.3 wt % ZrO_2), pure grade FeO (68.4 wt % FeO, 29.6 wt % Fe_2O_3, 0.5 wt % Fe), and high purity grade iron (>99.9 wt % Fe).

Test samples were prepared using induction melting in a cold crucible (IMCC) on Rasplav 2 and Rasplav 3 setups [17–19] in flowing argon. In order for iron oxide to crystallize in the wustite structure ($Fe_{1-x}O$) with the composition nearest to the FeO stoichiometry, more metallic iron was added as a getter in an amount of 1 wt % of the total sample weight (Fig. 1). We should note that this iron amount almost does not affect the liquidus temperature in the ZrO_2–FeO system because of the low iron solubility in the oxide melt (Fig. 1).
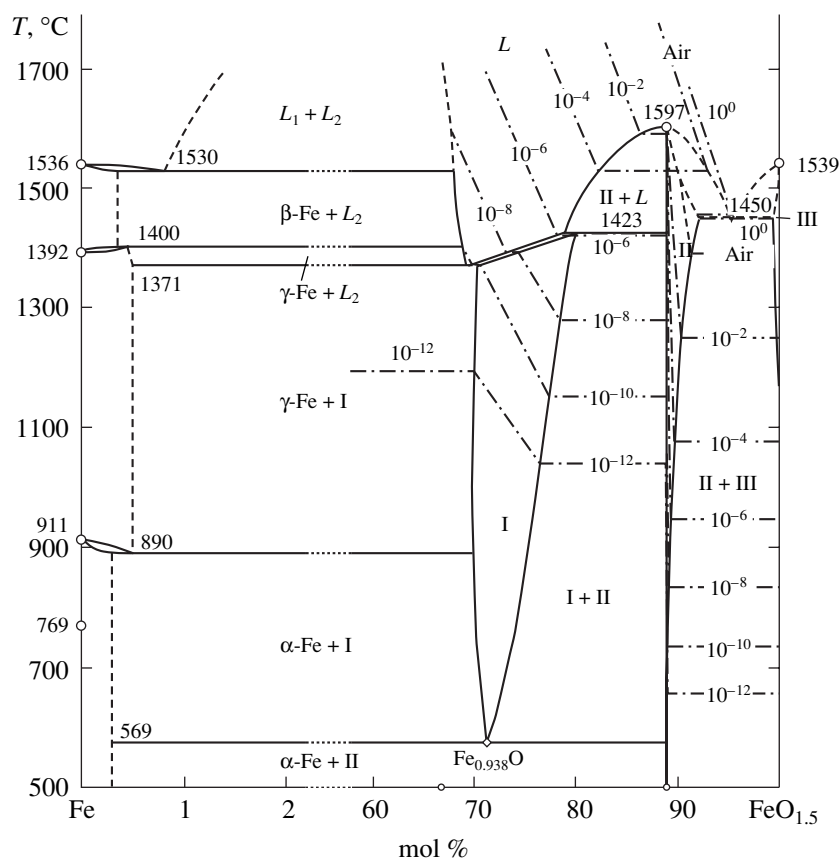
Fig. 1. Phase diagram for the Fe–Fe$_2$O$_3$ system compiled of the data from [8–13]. Notation: I—wustite phase; II—magnetite phase; III—hematite phase; L_1—liquid on the side of metallic iron; L_2—liquid on the FeO side; dashed lines—oxygen isobars.

The phase composition is controlled by means of X-ray powder diffraction (a DRON-3 diffractometer, CoK_α radiation).

The chemical composition of the samples is determined spectrophotometrically, gas-volumetrically [20–22], and by X-ray fluorescence analysis (a Spark 1M spectrometer).

The microstructure, the elemental composition of the samples, and the compositions of separate phases are determined using scanning electron microscopy (SEM) and energy-dispersive electron-probe microanalysis (EDX) on a CamScan MV2300 or ABT-55 scanning electron microscope equipped with Oxford Link microprobe attachments. The element determination error of this method varies with the atomic number of the element and averages ±0.3 wt %.

Thermal transformations in the system are studied using differential scanning calorimetry (DSC) on a Netzsch STA 429 thermal analyzer. The temperatures of thermal effects are determined as the onset temperatures of DSC peaks; the onset temperature of a peak is determined as the intersection of the tangents to the baseline and the curve. In the DSC experiments, we use corundum crucibles; the sample size is about 30 mg; the heating rate is 10 K/min; the atmosphere is inert (argon or helium). The solidus temperatures T_{sol} and the liquidus temperatures T_{liq} are also determined by visual polythermal analysis (VPA) using original equipment and techniques, namely, cold-crucible melting (VPA IMCC; Fig. 2a) [18] and Galakhov microfurnace (Fig. 2b) [23].

The VPA IMCC determinations of the liquidus temperatures are performed as follows: the temperature is measured at the surface of the melt pool at the moment when a solid phase appears in the sight field of a Raytek MR1-SC spectral-ratio pyrometer (Fig. 2a, *8*; the middle frame). The error of this method in the liquidus temperature determination, as a rule, does not exceed 50–75°C [24].

In the VPA experiments in Galakhov furnace, fragments of a IMCC-prepared ingot 7–8 mg in weight are mounted between the turns of the spiral holder that is placed in the isothermal zone of the microfurnace (Fig. 2b). The working range of temperature measurement in the microfurnace is 900–2500°C. The temperature measurement error is about ±30°C [23]. The measurements are carried out under an inert atmosphere (for the low-temperature region, high purity grade helium is used with a total pressure of 0.25×10^5 Pa in the system; for the high-temperature, an argon + hydro-
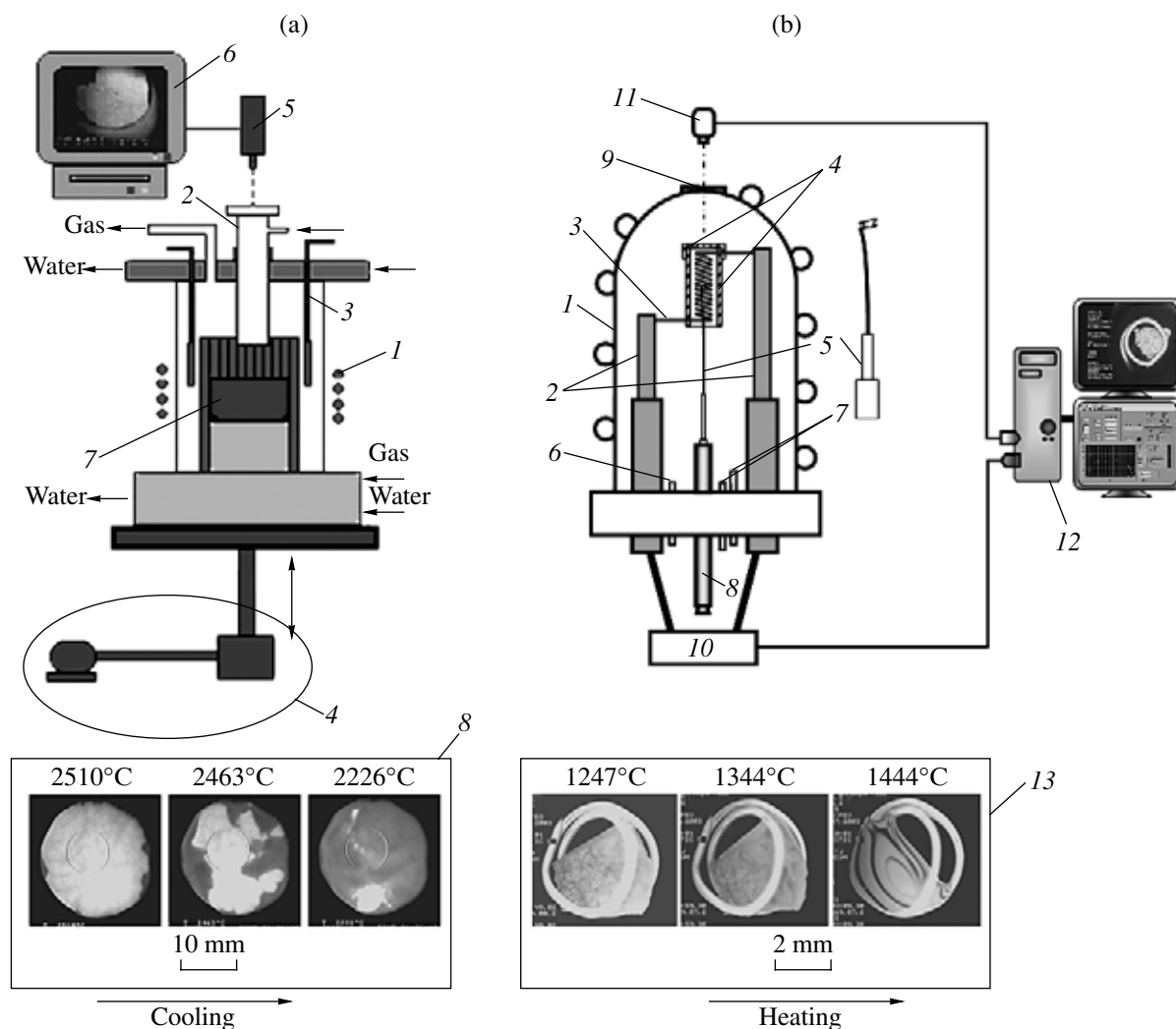
Fig. 2. Schematics of the VPA setups used. Panel (a): a Rasplav 3 IMCC setup: (*1*) inductor, (*2*) duct of the pyrometer, (*3*) movable water-cooled electromagnetic shield, (*4*) vertical drive of the crucible, (*5*) pyrometer combined with a video camera, (*6*) monitoring and control system, (*7*) melt, and (*8*) sight field of the melt pool surface during cooling. Panel (b): Galakhov microfurnace: (*1*) water-cooled vacuum housing, (*2*) steel electrodes, (*3*) tungsten heating coil, (*4*) molybdenum shields, (*5*) sample holder (made of iridium or molybdenum), (*6*) evacuation system, (*7*) gas admission system, (*8*) quenching device, (*9*) quartz glass window, (*10*) controlled power supply, (*11*) video camera, (*12*) monitoring and control system, and (*13*) sample in the holder during heating.

gen mixture (96/4 mol/mol) is used with a total pressure of 1.25×10^5 Pa in the system). To avoid a reaction of the sample with the holder, the holder is made of iridium. First, we study how the heating rate affects the error of the visual determination of the onset melting temperature and the final melting temperature and then choose an optimal rate in the vicinity of critical points (5 K/s); this is done to improve the precision of the determination of the solidus and liquidus temperatures in the dynamic mode. The melting of the sample is recorded with a digital video camera and is analyzed frame by frame. The solidus temperature is set equal to the temperature at which the geometrical form of the edges of the sample starts to degrade during heating. The liquidus temperature is set equal to the temperature at which the sample fully spreads over the surface of the

holder (Fig. 2b, *13*; the last frame). The design of Galakhov microfurnace enables us to quench samples by dropping them, together with the holder, into cold water. The microstructure and element composition of the constituent phases are determined after quenching.

RESULTS AND DISCUSSION

The compositions of the samples after IMCC determined by the chemical analysis and determined by EDX after the experiments in Galakhov microfurnace are listed in Table 1. This table displays the solidus and liquidus temperatures determined by VPA IMCC, VPA in Galakhov microfurnace, and DSC.

In view of the fact that the melt that appears upon heating well wets all of the crucible materials used,
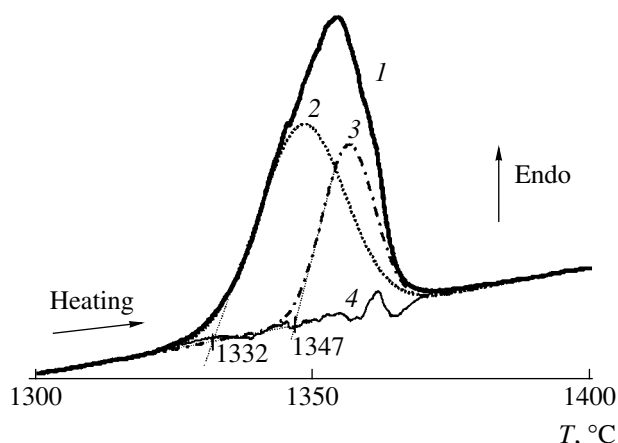
Fig. 3. DSC curve for a ZrO_2–FeO sample containing 10.5 mol % ZrO_2 (under inert atmosphere): (*1*) experimental curve, (*2*, *3*) decomposition of peak *1*, (*4*) difference between curve *1* and the sum of curves *2* and *3*.

reacts with oxide materials, and escapes from the crucible when its amount is large, a reliable DSC determination is possible only for the eutectic temperature. The thermoanalytical curves for the sample containing 10.5 ± 0.5 mol % ZrO_2 are shown in Fig. 3. The DSC data show that the test sample has a near-eutectic composition. However, the possibility to represent the endothermic peak in the form of two overlapping endotherms (Fig. 3, Table 1) means that the composi-

Table 1. Solidus and liquidus temperatures in the ZrO_2–FeO system

ZrO_2 mol %	Temperature, °C	
	solidus	liquidus
10.5[a]	1332[c]	1347[c]
13.7[a]	–	1591[d]
14.5[b]		1605[e]
19.7[a]		1797[d]
21.4[b]		1793[e]
31.6[a]		2040[d]
33.2[b]	1342[d]	2030[e]
33.6[b]	–	2020[e]
42.0[b]		2112[e]
44.8[b]		2161[e]
49.7[a]		2146[d]
58.7[a]		2331[d]
71.2[b]		2463[e]

Note: [a] EDX data. [b] Chemical analysis. [c] DSC data. [d] VPA data in Galakhov furnace. [e] VPA IMCC data.

tion of the sample slightly deviates from the eutectic point. The gap between the solidus and liquidus temperatures for this composition is 15°C. The first of the overlapping endotherms, which is observed at 1332°C, is due to the eutectic temperature. The second endotherm, which is observed at 1347°C, is associated with the departure of the composition from the eutectic.

The X-ray powder diffraction of this sample shows that the system in this case is a mixture of iron oxide (wustite $Fe_{1-x}O$) and t-ZrO_2(FeO) ss (Fig. 4, *a*).

Since the sample of a near-eutectic composition contains very fine crystals of the zirconia-based phase (Fig. 5a), an attempt to analyze the crystals using EDX would yield a highly overestimated iron oxide concentration in the ss. Therefore, to more exactly determine the FeO concentration in the ZrO_2-based phase, the regions of the sample in which rather large grains of the zirconia-based phases appeared as a result of solid-phase recrystallization at a near-eutectic temperature are analyzed by SEM/EDX (Fig. 5b, Table 2). The EDX of such regions shows that the maximal iron oxide concentration in the ZrO_2-based ss is 2.2 mol % at a nearly-solidus temperature (Fig. 5b, Table 2). The EDX of the FeO-based phase in the same sample shows no solubility of zirconia in this phase (Fig. 5b, Table 2).

The phase corresponding to the zirconia-based ss is found in almost all samples (see, e.g., Fig. 5c). However, the ss grains in most of the crystallized samples are too small for EDX to provide the precise determination of the composition. To more precisely determine the composition of the ss of FeO in ZrO_2, we carry out an additional experiment in which a ZrO_2(FeO) ss layer is grown by pulling the crucible with the melt from the inductor at a speed of 8−10 mm/h for 1 h at the surface temperature of the melt pool equal to 2030°C. The composition containing 33.2 mol % ZrO_2 is used in this experiment. The layer thickness formed by the crystallization of the ZrO_2(FeO) ss provides a more precise determination of the FeO solubility limit in ZrO_2 (Table 2).

X-ray powder diffraction shows FeO (wustite) and cubic ZrO_2(FeO) ss in the 33.2 mol % ZrO_2 sample (Fig. 4, *b*). The FeO phase is washed by concentrated hydrochloric acid from this sample. The X-ray diffraction pattern of the washed sample (Fig. 4, *c*) shows two phases, namely, the c-ZrO_2(FeO) ss major phase and the m-ZrO_2 minor phase. The ratio between the cubic and monoclinic ss phases calculated using the relationship found in [25] shows that the c-ZrO_2 + m-ZrO_2 mixture contains about 70% c-ZrO_2. The monoclinic zirconia, likely, appears upon cooling of the ingot as a result of a portion (mostly fine-grained) of the c-ZrO_2(FeO) ss decomposing to yield iron oxide and the subsequent transformation c-$ZrO_2 \longrightarrow t$-$ZrO_2 \longrightarrow m$-ZrO_2.
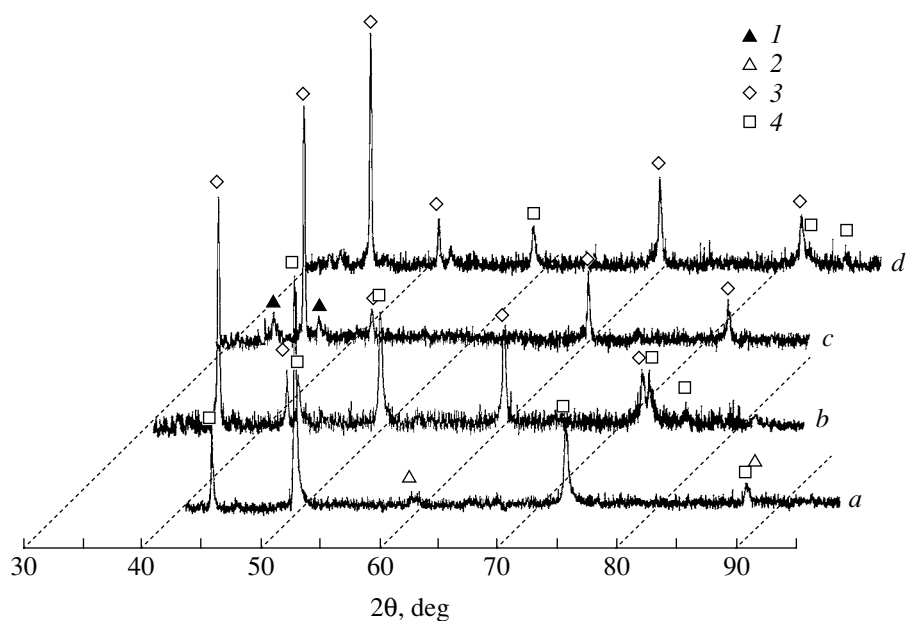
Fig. 4. X-ray diffraction patterns for ZrO$_2$–FeO samples with various zirconia concentrations: (*a*) a sample with 10.3 mol % ZrO$_2$, (*b*) a sample with 33.2 mol % ZrO$_2$ quenched from 2030°C, (*c*) ZrO$_2$(FeO) ss quenched from 2030°C (washed from the FeO-based phase), and (*d*) a sample with 58.7 mol % ZrO$_2$ quenched from 2300°C. Phase notation: (*1*) *m*-ZrO$_2$, (*2*) *t*-ZrO$_2$, (*3*) *c*-ZrO$_2$, and (*4*) FeO (wustite).
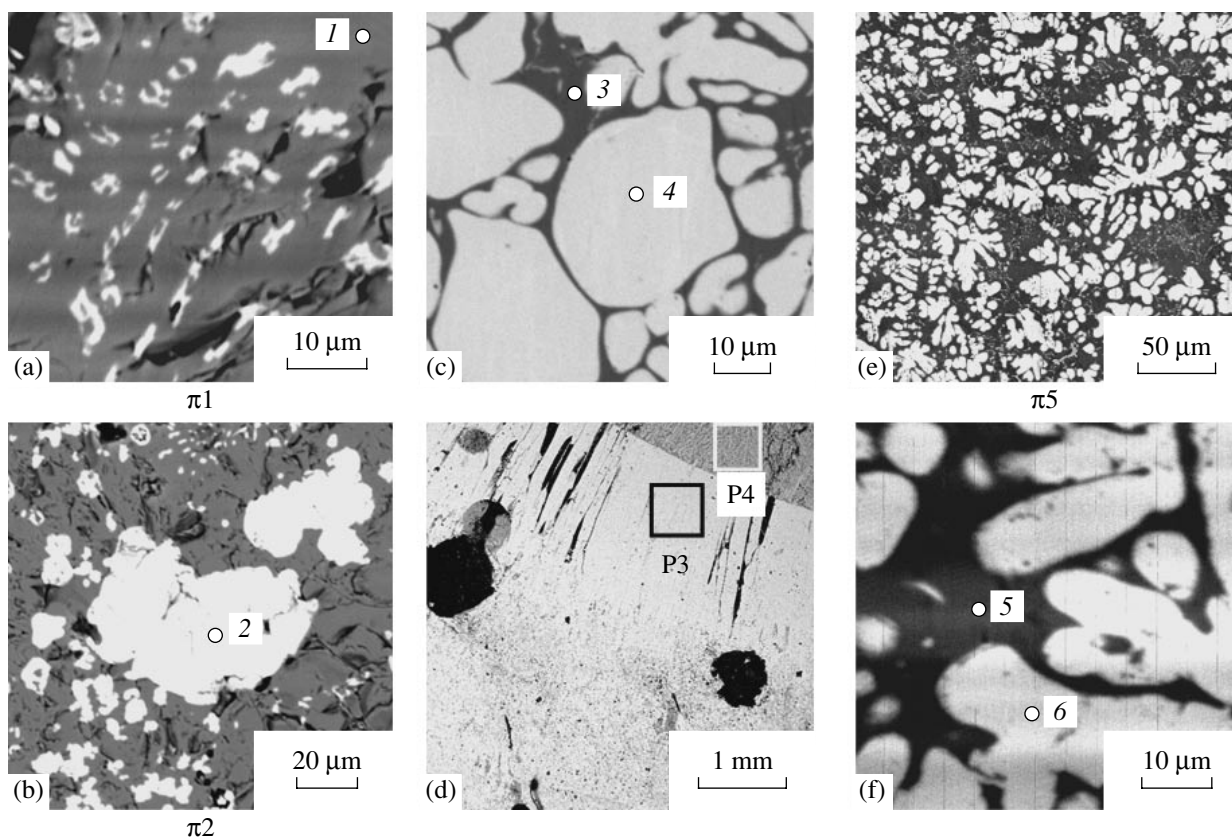

Fig. 5. Micrographs of crystallized ZrO$_2$–FeO samples with various zirconia concentrations: (a, b) samples with 10.3 mol % ZrO$_2$, (c) a sample with 33.2 mol % ZrO$_2$ quenched from 2030°C, (d) a sample with 33.2 mol % ZrO$_2$ pulled from the inductor, and (e, f) samples with 58.7 mol % ZrO$_2$ quenched from 2300°C.

Table 2. Chemical composition of the regions indicated in Fig. 5

mol % ZrO_2 in the sample	Region	Component, mol %	
		ZrO_2	FeO
10.3	*1*	–	100
	2	97.8	2.2
	P1	10.3	89.7
	P2	10.2	89.8
33.2	*3*	–	100
	4	88.3	11.7
	P3	87.1	12.9
	P4	31.6	68.4
58.7	*5*	–	100
	6	90.5	9.5
	P5	58.4	41.6

Using chemical analysis and X-ray diffraction data for this sample, taking into account that almost all iron oxide in this sample exists in c-ZrO_2(FeO) ss (Fig. 4, *c*), and taking into account the fraction of cubic zirconia in the c-ZrO_2 + m-ZrO_2 mixture, we may estimate the FeO concentration in c-ZrO_2(FeO) as 10.5 mol % FeO. Note that this estimate correlates with the data listed in Table 2.

The sample containing 58.7 mol % ZrO_2 and quenched from the liquidus temperature (2300°C) is studied by SEM/EDX and X-ray powder diffraction. The microstructure and composition of crystalline phases are shown in Fig. 5e, Fig. 5f, and Table 2. The X-ray diffraction pattern of this sample (Fig. 4, *d*) indicates that the ZrO_2-based ss crystallizes in the cubic phase in this temperature range, as the sample containing 33.2 mol % ZrO_2.

The parameters of the cubic and tetragonal zirconia-based ss are listed in Table 3.

An examination of the data compiled in Table 3 shows that the unit cell parameters decrease slightly as the FeO concentration of the c-ZrO_2(FeO) ss increases.

On the basis of the compositions and the solidus and liquidus temperatures determined using different methods (Tables 1, 2) and on the basis of the structures of the zirconia-based phases, we designed a phase diagram for the ZrO_2–FeO system (Fig. 6). The different methods yield consistent values of the solidus and liquidus temperatures, which verifies the adequacy of the results.

The liquidus trend, DSC data (Fig. 3), and SEM/EDX data (Fig. 5a, Table 2; region P2) prove that the eutectic in the ZrO_2–FeO system occurs at 1332 ± 5°C and 10.3 ± 0.6 mol % ZrO_2. Note that our composition of the eutectic differs appreciably from the Fischer and Hoffman data [16] (Fig. 6).

The c-ZrO_2(FeO) ss is detected in many runs; however, the lower existence boundary needs refinement. From the trend of the liquidus in the ZrO_2–FeO system, we may suggest that the cubic zirconia-based ss transforms to the tetragonal ss at a temperature lower than or equal to 1800°C. The iron oxide solubility in m-ZrO_2 is likely too low to be detected by either EDX or X-ray

Table 3. Structural parameters of ZrO_2(FeO) ss

mol % FeO in ZrO_2-based ss	Structure	Unit cell parameters, Å	Unit cell volume, Å^3
2.2*	Tetragonal	$a = 5.07 \pm 0.02$	132.8 ± 1.4
		$c = 5.17 \pm 0.03$	
0*** (17–923)		$a = 5.12$	137.63
		$c = 5.25$	
11.3 ± 0.5*	Cubic	$a = 5.085 \pm 0.006$	131.4 ± 0.5
10.5**		$a = 5.09 \pm 0.04$	132 ± 3
9.3 ± 0.2*		$a = 5.08 \pm 0.01$	131 ± 1
0*** (27–997)		$a = 5.09$	132.97

Notes: * EDX (Table 2).
     ** Chemical analysis of a sample washed from the FeO-based phase.
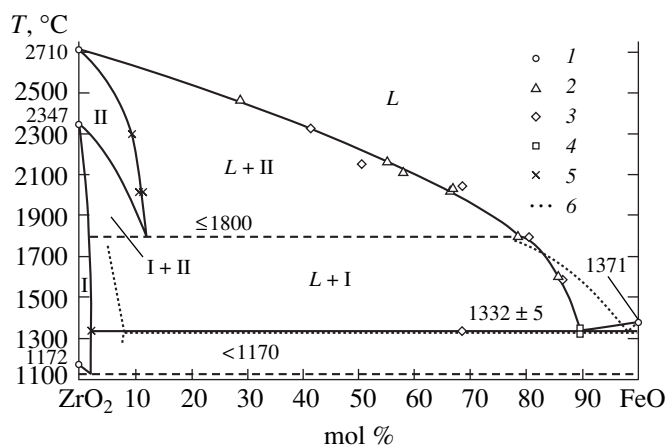   *** ASTM data.

Fig. 6. Phase diagram of the ZrO$_2$–FeO system (under an inert atmosphere): (*1*) reference data [8], (*2*) VPA IMCC, (*3*) VPA in Galakhov microfurnace, (*4*) DSC, (*5*) IMCC/EDX, and (*6*) data from [16]. Phase notation: I— *t*-ZrO$_2$(FeO) ss; II—*c*-ZrO$_2$(FeO) ss.

crystallography (unit cell parameter determinations). This confirms the Fischer and Hoffman data [16].

CONCLUSIONS

We have constructed a quasi-binary phase diagram for the ZrO$_2$–FeO system under an inert atmosphere (argon). This is a diagram with eutectic and limited solid solutions of FeO in ZrO$_2$. We have refined the temperature and composition of the eutectic, which lies at 10.3 ± 0.6 mol % ZrO$_2$ and 1332 ± 5°C.

We have determined the parameters of the end-members of the FeO solid solutions in ZrO$_2$. *c*-ZrO$_2$(FeO) exists over a temperature range of 2710–1800°C; the maximal solubility of FeO in ZrO$_2$ at ~1800°C is ~13 mol % FeO. *t*-ZrO$_2$(FeO) exists over a temperature range of 2347–1172°C; the maximal solubility of FeO in ZrO$_2$ is 2.2 ± 0.3 mol % at 1332°C.

ACKNOWLEDGMENTS

REFERENCES

1. L. G. Nekhamkin, Yu. A. Tsylov, M. N. Butova, *et al.*, in *Production of Rare Metals and Semiconductor Materials. A Survey* (TsNIITsVETMET, Moscow, 1989), No. 1, p. 25 [in Russian].
2. S. I. Filippov, S. P. Arsen'ev, V. V. Yakovlev, *et al.*, *The Physicochemical Investigation Methods of Metallurgical Processes* (Metallurgiya, Moscow, 1968) [in Russian].
3. T. G. Theofanous, C. Lin, S. Addition, *et al.*, Nucl. Eng. Des. **169** (1), 1 (1997).
4. S. V. Bechta, V. B. Khabensky, S. A. Vitol, *et al.*, Nucl. Eng. Des. **210** (1–3), 193 (2001).
5. V. V. Gusarov, V. I. Al'myashev, S. V. Beshta, *et al.*, Teploenergetika **49** (9), 22 (2001).
6. V. V. Gusarov, V. I. Al'myashev, V. B. Khabenskii, *et al.*, Fiz. Khim. Stekla **31** (1), 71 (2005).
7. V. A. Rabinovich and Z. Ya. Khavin, *The Concise Chemical Handbook* (Khimiya, Leningrad, 1978) [in Russian].
8. L. V. Gurvich, V. S. Iorish, D. V. Chekhovskoi, and V. S. Yungman, *IVTANTHERMO: A Thermodynamical Database and Software System for the Personal Computer. User'S Guide* (CRC Press, Boca Raton, FL, 1993).
9. L. S. Darken and R. W. Gurry, J. Am. Chem. Soc. **67** (8), 1398 (1945).
10. L. S. Darken and R. W. Gurry, J. Am. Chem. Soc. **68** (5), 798 (1946).
11. P. E. C. Bryant and W. W. Smeltzer, J. Electrochem. Soc. **116**, 1409 (1969).
12. O. Kubaschewski, *Iron: Binary Phase Diagrams* (Springer, Berlin, 1982), p. 79.
13. P. T. Carter and M. Ibrahim, J. Soc. Glass Technol. **36** (170), 142 (1952).
14. N. A. Toropov, V. P. Barzakovskii, I. A. Bondar', *et al.*, *Phase Diagrams of Silicate Systems. Handbook*, Vol. 2: *Metal–Oxygen Compounds of Silicate Systems* (Nauka, Leningrad, 1969) [in Russian].
15. N. A. Toropov, V. P. Barzakovskii, V. V. Lapin, and N. N. Kurtseva, *Phase Diagrams of Silicate Systems. Handbook*, Vol. 1: *Binary Systems* (Nauka, Moscow, 1965) [in Russian].
16. W. A. Fischer and A. Hoffmann, Arch. Eisenhuttenwesen **28**, (11), 739 (1957).
17. Yu. B. Petrov, *Induction Melting of Oxides* (Energoatomizdat, Leningrad, 1983) [in Russian].
18. D. Lopukh, S. Bechta, A. Pechenkov, *et al.*, in *Proceedings of the 8th International Conference on Nuclear Engineering (ICONE-8), Baltimore, 2000* (Baltimore, 2000), ICONE-8139.
19. L. M. Viting, *High-Temperature Solutions and Melts* (Mosk. Gos. Univ., Moscow, 1991) [in Russian].
20. *The Russian State Standard (GOST) 4011-72*: *Potable Water. The Measurements of the Weight Concentration of Total Iron.*
21. E. Sandell, *Colorimetric Determination of Traces of Metals* (New York, 1959; Mir, Moscow, 1964).
22. B. G. Eremina, *Gas Analysis* (Goskhimizdat, Leningrad, 1955) [in Russian].
23. F. Ya. Galakhov, in *Advanced Investigations of Silicates and Civil Building Materials* (Gosstroiizdat, Moscow, 1961), p. 178 [in Russian].
24. M. V. Pikunov, *Metal Alloying, Alloy Crystallization, Cast Solidification* (MISIS, Moscow, 1997) [in Russian].
25. O. V. Pozhidaeva, E. N. Korytkova, I. A. Drozdova, and V. V. Gusarov, Zh. Obshch. Khim. **69** (8), 1265 (1999).